Article

Heterointerface Engineered Core-Shell Fe$_2$O$_3$@TiO$_2$ for High-Performance Lithium-Ion Storage

Zeqing Miao [1], Kesheng Gao [1], Dazhi Li [2], Ziwei Gao [1], Wenxin Zhao [2], Zeyang Li [2], Wei Sun [2], Xiaoguang Wang [3], Haihang Zhang [3], Xinyu Wang [3], Changlong Sun [2], Yuanyuan Zhu [4],[*] and Zhenjiang Li [2],[*]

[1] Shandong Engineering Laboratory for Preparation and Application of High-Performance Carbon-Materials, College of Electromechanical Engineering, Qingdao University of Science and Technology, Qingdao 266061, China

[2] College of Materials Science and Engineering, Qingdao University of Science and Technology, Qingdao 266042, China

[3] Sino-German Institute of Technology, Qingdao University of Science and Technology, Qingdao 266100, China

[4] Key Laboratory of Spin Electron and Nanomaterials of Anhui Higher Education Institutes, Suzhou University, Suzhou 234000, China

[*] Correspondence: zhuyy@ahszu.edu.cn (Y.Z.); zhenjiangli@qust.edu.cn (Z.L.)

Abstract: The rational design of the heterogeneous interfaces enables precise adjustment of the electronic structure and optimization of the kinetics for electron/ion migration in energy storage materials. In this work, the built-in electric field is introduced to the iron-based anode material (Fe$_2$O$_3$@TiO$_2$) through the well-designed heterostructure. This model serves as an ideal platform for comprehending the atomic-level optimization of electron transfer in advanced lithium-ion batteries (LIBs). As a result, the core-shell Fe$_2$O$_3$@TiO$_2$ delivers a remarkable discharge capacity of 1342 mAh g^{-1} and an extraordinary capacity retention of 82.7% at 0.1 A g^{-1} after 300 cycles. Fe$_2$O$_3$@TiO$_2$ shows an excellent rate performance from 0.1 A g^{-1} to 4.0 A g^{-1}. Further, the discharge capacity of Fe$_2$O$_3$@TiO$_2$ reached 736 mAh g^{-1} at 1.0 A g^{-1} after 2000 cycles, and the corresponding capacity retention is 83.62%. The heterostructure forms a conventional p-n junction, successfully constructing the built-in electric field and lithium-ion reservoir. The kinetic analysis demonstrates that Fe$_2$O$_3$@TiO$_2$ displays high pseudocapacitance behavior (77.8%) and fast lithium-ion reaction kinetics. The capability of heterointerface engineering to optimize electrochemical reaction kinetics offers novel insights for constructing high-performance iron-based anodes for LIBs.

Keywords: lithium-ion storage; iron-based anode; heterointerface engineering; built-in electric field; electrochemical kinetics

1. Introduction

The increasing popularity of new-energy trams and the growing market demand for new-energy electronic devices have rendered electrochemistry and its related fields indispensable to the advancement of energy technology [1–3]. The advantages of no memory effect, extended lifespan, high energy density, and superior safety make lithium-ion batteries (LIBs) a prospective technology choice for future large-scale applications [4–8]. However, the limited theoretical capacity (372 mAh g^{-1}) and inadequate rate performance of commercial graphite anodes impede the advancement of LIBs [9–11]. By identifying suitable anode materials to enhance capacity and kinetics, LIBs could offer superior energy/power density and broader application prospects. Transition metal oxides (TMOs), especially Fe$_2$O$_3$ with its high theoretical capacity (1007 mAh g^{-1}) [12], abundance, strong chemical stability, and eco-friendliness, have attracted considerable interest [13–18]. However, the high lithiation potential, significant volume expansion, and side reaction tendencies diminish the feasibility of Fe$_2$O$_3$ as an LIB anode [19]. The use of frame support or core-shell structures to limit the volume expansion of Fe$_2$O$_3$ has proven to be an effective strategy. For example,

Qi et al. synthesized Fe_2O_3/graphene nanocomposites by the high-pressure hydrothermal method, achieving a capacity of 1100.5 mAh g^{-1} at 0.2 A g^{-1} after 350 cycles [20]. Wang et al. developed $C@Fe_2O_3$/SWCNT nanocomposites, demonstrating favorable lithium-ion storage capacity with a reversible capacity of 1294.7 mAh g^{-1} at 0.05A g^{-1} [21]. He et al. prepared Fe_2O_3/C/rGO nanomaterials by the physical crosslinking method, attaining a reversible capacity of 609 mAh g^{-1} at 1.0 A g^{-1} while exhibiting excellent power density [22]. Although the strategy of composite or hybrid with carbon-based materials has proven effective in stabilizing electrochemical reactions and preventing physical crushing of Fe_2O_3 during lithiation/delithiation, some effective electron transfer is still sacrificed due to poor kinetics. Furthermore, the inadequate conductivity of Fe_2O_3 results in the significant polarization and degradation of lithium-ion storage performance at high current densities [23,24]. Therefore, the structure design and interface effect of Fe_2O_3 anodes are essential for high lithium-ion storage capacity.

Recognized for its remarkable structural stability, TiO_2 has been dubbed a "zero-stress material" [25]. Compared to carbon-based materials, TiO_2 possesses a higher lithium-ion inserting potential (1.5 V–1.8 V) and is less susceptible to the electroplating effect [25], thus TiO_2 is often regarded as a safer choice for anode materials in LIBs. However, the low theoretical capacity of merely 167.5 mAh g^{-1} and inferior rate performance have impeded the research advancement of TiO_2 [26]. Guan et al. designed S-doped $TiO_2@C$ nanosheets, achieving a capacity of 550 mAh g^{-1} at 0.3 C and a stable cycling life of 85.8% after 1000 cycles [27]. Hao et al. constructed O-deficient TiO_2 with abundant active lithium-ion storage sites, offering a reversible capacity of 50 mAh g^{-1} at 100 C [28]. Xia et al. reported black TiO_2 with a disordered surface could reach a remarkable reversible capacity of ~120 mAh g^{-1} at 0.04 C after 500 cycles [26]. Despite these advances, the sluggish lithium-ion diffusion kinetic remains a primary impediment constraining the lithium-ion storage capacity of TiO_2. Constructing a heterostructure by coupling Fe_2O_3 and TiO_2 represents an efficacious strategy for enhancing individual anode performance in lithium-ion storage. Fe_2O_3, an exemplary n-type semiconductor, and TiO_2, a p-type semiconductor, form a heterostructure that triggers spontaneous electron movement towards the n-type semiconductor due to an electron concentration difference, leading to the creation of a built-in electric field at the heterointerface [29]. This built-in electric field can effectively improve the lithium-ion reaction kinetics, maintain long-term cycle stability, and maximize the synergistic effect of the heterostructure [30]. Therefore, the construction of a heterostructure signifies an optimal solution for augmenting the lithium-ion storage capacity of individual anodes (Fe_2O_3 or TiO_2).

In this work, we propose feasible heterointerface engineering to fabricate a core-shell $Fe_2O_3@TiO_2$ heterostructure as an advanced anode for LIBs through solvothermal and sol-gel progress. As expected, the well-designed $Fe_2O_3@TiO_2$ heterostructure demonstrates remarkable lithium-ion storage performance, achieving an ultrahigh rate capacity, extraordinary cycling performance (1342 mAh g^{-1} at 0.1A g^{-1} after 300 cycles), and superior cycling durability (capacity retention of 83.6% at 1.0 A g^{-1} after 2000 cycles). The improvement of electrochemical kinetics for the $Fe_2O_3@TiO_2$ heterostructure is confirmed by pseudocapacitance and electrochemical impedance spectroscopy (EIS). Our work fully exploits the synergistic effects of heterogeneous interfaces to enhance lithium-ion reaction kinetics and improve cycle durability, thereby providing valuable ideas for designing rational interface engineering and manufacturing advanced energy storage devices.

2. Results

The detailed process route of the $Fe_2O_3@TiO_2$ heterostructure is illustrated in Figure S1. The $Fe_2O_3@TiO_2$ heterostructure is qualitatively examined by X-ray powder diffraction (XRD), initially. As shown in Figure 1a, the diffraction peaks located at 24.2°, 33.2°, 35.6°, 40.9°, 49.5°, 54.1°, 56.2°, 57.7°, 62.6°, and 64.1° can be indexed to (012), (104), (110), (113), (024), (116), (211), (018), (214), and (300) crystal planes of α-Fe_2O_3, respectively (PDF#89-0599). The diffraction peaks of the $Fe_2O_3@TiO_2$ heterostructure and Fe_2O_3 particles exhibit

negligible deviation from the standard cards, thereby confirming the successful synthesis of high-purity α-Fe_2O_3. Additionally, the diffraction peaks located at 25.3°, 36.9°, 37.9°, 38.6°, 48.1°, 55.1°, 62.7°, 68.8°, 70.4°, and 75.1° can correspond to (101), (103), (004), (112), (200), (211), (204), (220), and (215) crystal planes of anatase-TiO_2 (PDF#71-1166), respectively. XRD results indicate that the $Fe_2O_3@TiO_2$ heterostructure, Fe_2O_3 particles, and TiO_2 particles have good crystallinity. Furthermore, the structure of the $Fe_2O_3@TiO_2$ heterostructure is analyzed by transmission electron microscopy (TEM). The core-shell structure, as illustrated in Figure 1b, is distinguishable, with Fe_2O_3 particles completely wrapped by TiO_2 (Figure 1c,d). Further, the selected area electron diffraction (SAED) of the $Fe_2O_3@TiO_2$ heterostructure is shown in Figure 1e, revealing the $Fe_2O_3@TiO_2$ heterostructure to be comprised of multiple nanocrystals and exhibiting excellent crystallinity, which aligns with the XRD results. A particle with a small shell thickness is selected to analyze the outer TiO_2 shell, as shown in Figure 1f. The corresponding HRTEM image is presented in Figure 1g, exhibiting well-defined lattice fringes characteristic of the (101) crystal plane of anatase-TiO_2, with a measured lattice spacing of 0.35 nm. In Figure 1h, distinct nanocrystals are observed, with the left lattice spacing of 0.35 nm corresponding to the (101) crystal plane of anatase-TiO_2 and the right lattice spacing of 0.23 nm corresponding to the (004) crystal plane of anatase-TiO_2, indicating that the outer shell comprises multiple anatase-TiO_2 nanocrystals. In addition, a substantial abundance of disordered structures is observed within the outermost layer (Figure 1i), exhibiting similarities to previously reported black TiO_2 [26]. The disordered surface facilitates the transition of Ti 2p orbital electrons to 3d orbitals, making it easier to capture charge carriers and improve the overall conductivity of TiO_2 [31]. Furthermore, the presence of a significant quantity of disordered nanocrystals in TiO_2 generates an intermediate energy state within the band gap, exhibiting a distinct energy distribution compared to the defect of crystals [32]. The contribution lies in the narrowing of the band-gap width and the enhancement of electrochemical kinetics [26]. Additionally, the elemental mapping results in Figure S2 reveal the homogeneous distribution of Fe, Ti, and O elements in $Fe_2O_3@TiO_2$, whereby the Fe element is mainly provided by internal Fe_2O_3, Ti comes from the shell of TiO_2, and O is derived from the Fe_2O_3, TiO_2, and adsorbed oxygen. The surface element composition and valence state of $Fe_2O_3@TiO_2$ heterostructure are analyzed by X-ray photoelectron spectroscopy (XPS). The presence of Ti, O, and Fe elements in Figure 1j can be determined based on the precise localization of characteristic peaks, without any indication of the existence of other impurity elements. The high-resolution XPS spectrum of the Fe 2p orbit is further presented in Figure 1k, the peak located at 722.9 eV corresponds to Fe $2p_{1/2}$, the peak located at 709.3 eV corresponds to Fe $2p_{3/2}$, and the small characteristic peak between Fe $2p_{1/2}$ and Fe $2p_{3/2}$ can be indexed to the satellite peak of Fe^{3+} [33]. The high-resolution XPS spectrum of the Ti 2p orbit is presented in Figure 1l. The peaks observed at 463.2 eV and 457.6 eV are attributed to the $2p_{1/2}$ and $2p_{3/2}$ orbitals of Ti, respectively [33]. Moreover, the high-resolution XPS spectrum of the O 1s orbit in Figure 1m exhibits well-defined peaks at 529.8 eV and 528.7 eV, corresponding to the Fe-O and Ti-O bonds, respectively [33]. These XPS results provide compelling evidence for the successful synthesis of both Fe_2O_3 and TiO_2.

The crystal structure of α-Fe_2O_3, corresponding to a rhomboidal crystal system, is depicted in Figure 2a. The standard half-cell test procedure is employed to conduct the testing of Fe_2O_3. To elucidate the underlying mechanism of lithium-ion storage, an initial cyclic voltammetry (CV) test is performed (Figure 2b). The significant reduction reaction occurs at 0.61 V during the initial discharge process, which can be interpreted as the formation mechanism of the solid electrolyte interphase (SEI) film [34]. During the initial charge process, a distinct oxidation peak is observed between 1.4 V to 2.26 V, indicating a continuous Fe^0 to Fe^{3+} oxidation process, consistent with previous reports [34]. The CV curves of the second and third cycles exhibit a remarkable alteration compared to that of the first cycle. During the discharge process, a novel reduction peak emerges at 0.92 V, indicating an electrochemical reaction described by Equation (1) [35].
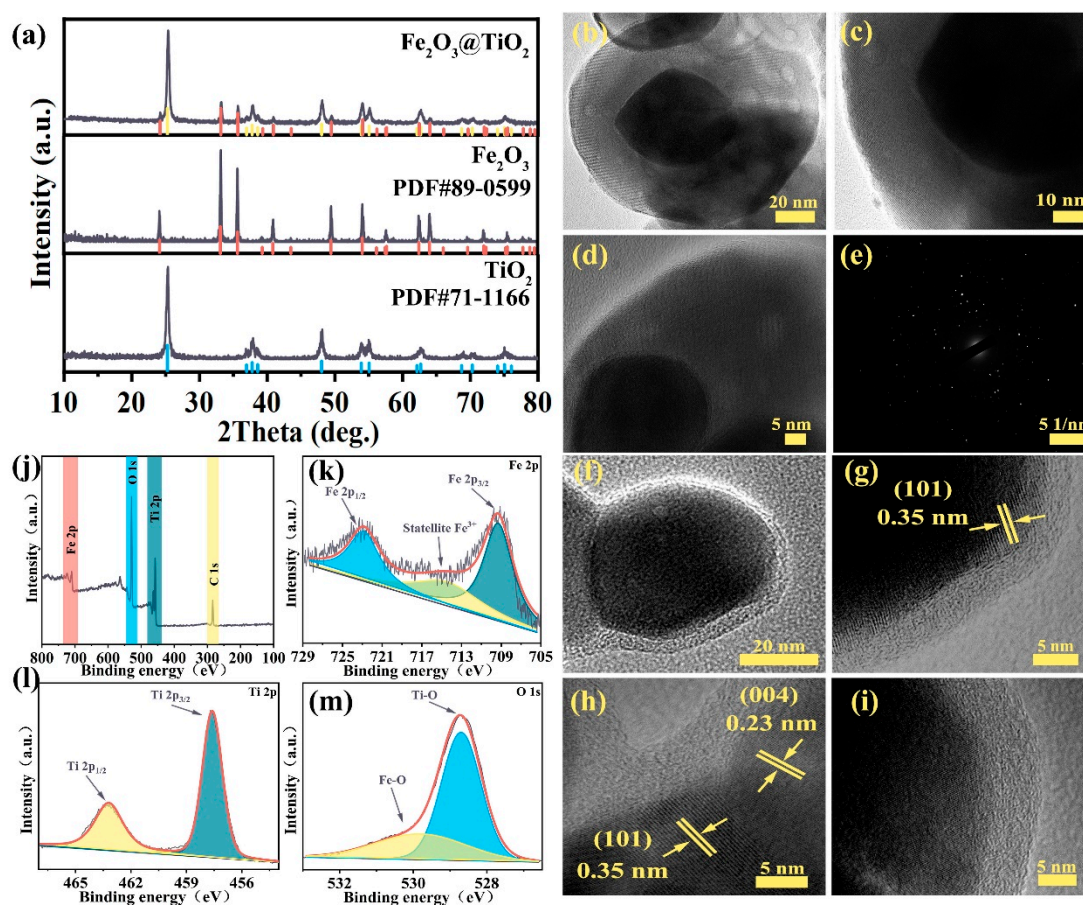
$$Fe_2O_3 + 6Li^+ + 6e^- \rightarrow 2Fe^0 + 3Li_2O \tag{1}$$
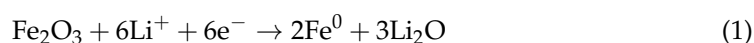
Figure 1. Characterization of Fe$_2$O$_3$@TiO$_2$ heterostructure: (**a**) XRD patterns; (**b**–**i**) TEM, SAED, and HRTEM images; (**j**) XPS survey spectrum and high-resolution XPS survey spectra of (**k**) Fe 2p orbital, (**l**) Ti 2p orbital, and (**m**) O 1s orbital.
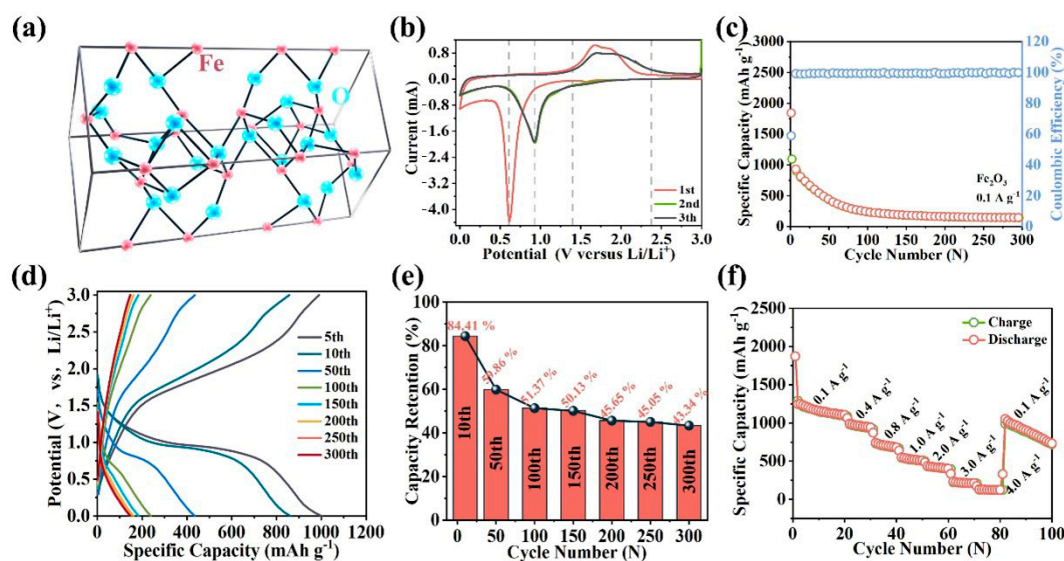

Figure 2. (**a**) Crystal structure image of α-Fe$_2$O$_3$. Electrochemical properties of Fe$_2$O$_3$ as anode material for LIBs: (**b**) CV curves at a scan rate of 0.1 mV s^{-1}; (**c**) cycling performance at a current density of 0.1 A g^{-1}, (**d**) GCD curves, (**e**) capacity retention and linear fit curve; (**f**) rate performance from 0.1 A g^{-1} to 4.0 A g^{-1}.

Additionally, compared to the charging process of the initial cycle, a discernible shift toward higher voltage is observed in the oxidation. This shift may be attributed to a polarization phenomenon caused by surface-insulating lithium compounds [36]. The half-cell is tested at 0.1 A g^{-1} for the cycle performance (Figure 2c). The discharge capacity reaches 1844.6 mAh g^{-1}, while the charge capacity amounts to 1095.1 mAh g^{-1} in the first cycle, resulting in an initial Coulombic efficiency (ICE) of 59%. The ultra-high ICE indicates a substantial conversion of lithium-ion into irreversible Li-containing compounds during the initial charge/discharge process [37]. Indeed, the capacity exhibits a declining trend over 300 cycles, with the capacity dropping to only 146.8 mAh g^{-1} at the 300th cycle. To explore the reason for the capacity decrease, the GCD curves are analyzed in Figure 2d. The voltage platform exhibits a pronounced decline and eventually diminishes during the repeated charge/discharge process, indicating the deactivation of the initial electrochemical reaction. The capacity retention exhibits a significant decline in Figure 2e, with a mere 14.66% remaining at the 300th cycle, indicating the gradual failure of Fe^{3+} and a corresponding decrease in effective electron transfer. The results of the capacity retention are consistent with the GCD curves. Furthermore, the rate performance of the Fe_2O_3 anode is examined in Figure 2f, ranging from 0.1 A g^{-1} to 4.0 A g^{-1}. Remarkably, at the 20th cycle, the discharge capacity reaches an impressive value of 1108 mAh g^{-1}. Upon reaching a current density of 0.1 A g^{-1}, the discharge capacity reverts to 1049 mAh g^{-1}, leading to a significant decrease. Ultimately, the discharge capacity only reaches 731 mAh g^{-1} after the 100th cycle, indicating a suboptimal rate capacity of Fe_2O_3. Moreover, the Fe_2O_3 anode is tested in a long-term cycle at 1.0 Ag^{-1}, as shown in Figure S3a. The initial discharge capacity stands at 1479.5 mAh g^{-1}, while the first charge capacity reaches 981.5 mAh g^{-1}, with an ICE of 66%. The discharge capacity exhibits a continuous decline with repeated charge/discharge, ultimately reaching only 99 mAh g^{-1} after 2000 cycles. The capacity retention depicted in Figure S3b accurately represents the electrochemical behavior of the Fe_2O_3 anode. The capacity retention gradually decreases to 32% until the 35th cycle, followed by a relatively stable retention from the 35th cycle to the 1200th cycle. Eventually, the capacity retention drops to 12.23% at the 2000th cycle. Combined with the electrochemical test results, the Fe_2O_3 anode can deliver extremely high capacity, but it cannot be maintained. The primary cause lies in the gradual deactivation of Fe^{3+} during repeated charge/discharge cycles, which arises from the pronounced volume expansion during repeated lithiation/delithiation.

The crystal structure of anatase-TiO_2 is shown in Figure 3a. The electrochemical performances of the TiO_2 anode are analyzed by a standard half-cell test process. Figure 3b shows the CV curves of TiO_2 anode at a scan rate of 0.1 mV s^{-1}. The reduction peak observed at 1.52 V in the initial discharge process can be regarded as the lithium-ion insertion, as exemplified by Equation (2) [28].

$$TiO_2 + xLi^+ xe^- \rightarrow Li_xTiO_2 \qquad (2)$$
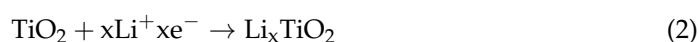
The emergence of the second reduction peak at 0.7 V can be attributed to the formation of the SEI film on the surface [38]. During the charge process, the oxidation peak located at 1.6 V corresponds to the process of lithium-ion desertion [38]. The CV curves of the second and third cycles exhibit a remarkable fit, thereby indicating the inherent stability of the electrochemical reaction. Figure 3c shows the cycling performance of the TiO_2 anode at 0.1 A g^{-1}. In the first charge/discharge process, the discharge capacity reaches 605.3 mAh g^{-1}, the charge capacity reaches 450.7 mAh g^{-1}, and the corresponding ICE is 74%. The exceptional discharge capacity can be ascribed to the disordered surface, offering an abundance of active lithium-ion storage sites [26]. The discharge capacity exhibits a continuous decline from the initial cycle to the 50th cycle, which could be related to the activation process of TiO_2. The discharge capacity exhibits minimal fluctuations over the subsequent 250 cycles and eventually maintains 205 mAh g^{-1} at the 300th cycle. The extraordinary cycle durability can be attributed to the enhanced structural adaptability of the disordered surface during charge/discharge processes [26]. Further, the GCD curves

of TiO_2 are shown in Figure 3d. The excellent degree of curve fitting indicates minimal polarization. The electrochemical stability of TiO_2 is demonstrated by the maintenance of a distinct voltage plateau over more than 300 cycles. Figure 3e shows the capacity retention at 0.1 A g^{-1}, which remains stable at 50% after 100 cycles. The rate performance of the TiO_2 anode is shown in Figure 3f. The discharge capacity reaches 281 mAh g^{-1} at the 20th cycle at 0.1 A g^{-1}. Upon restoring the current density to 0.1 A g^{-1}, the discharge capacity returns to 315 mAh g^{-1} and exhibits sustained stability. The stability demonstrated by the rate capacity is consistent with the capacity retention, which can be attributed to the reduction in the energy barrier of lithium-ion transport in the disordered surface of the TiO_2 [39]. Moreover, the long-term cycle test is shown in Figure S4a. The discharge capacity of 172.3 mAh g^{-1} can still be achieved after 2000 cycles at 1.0 A g^{-1}, and the Coulomb efficiency is always maintained at ~100%. In Figure S4b, the cycle durability of TiO_2 is further observed by calculating the capacity retention. The capacity retention of the 10th cycle is 83.63%. The capacity retention exhibits a slight decline from the 10th to the 200th cycle, followed by an increase to approximately 85%. Finally, the capacity retention is still maintained at 82.63% in the 2000th cycle. In conjunction with the findings from the aforementioned electrochemical tests, the TiO_2 anode exhibits exceptional cycling durability, a stable electrochemical reaction process, and minimal polarization phenomenon, thereby effectively mitigating volume expansion and enhancing electrical conductivity.
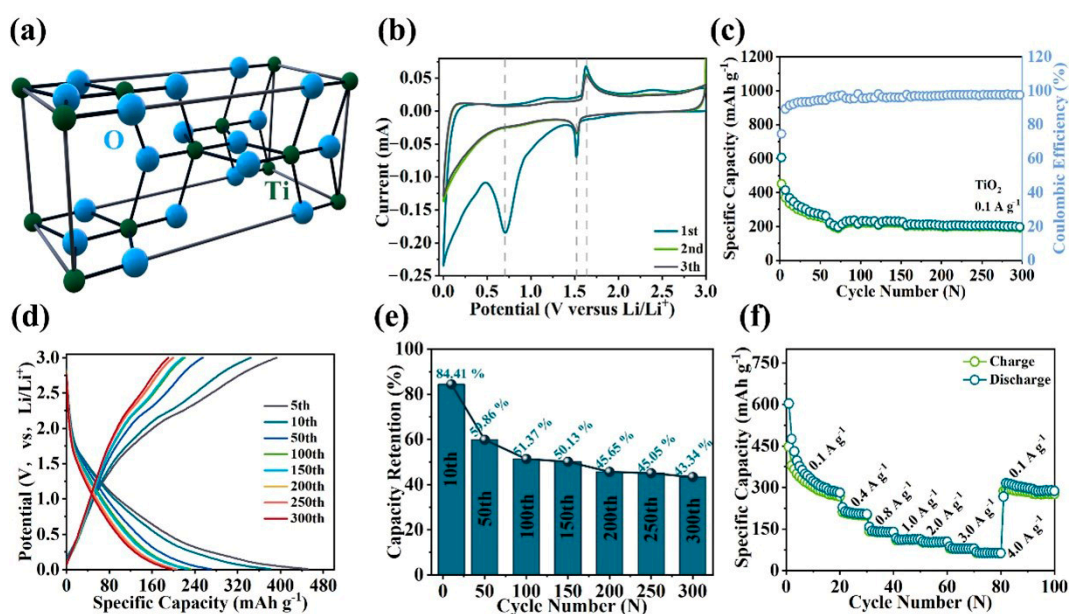

Figure 3. (**a**) Crystal structure image of anatase-TiO_2. Electrochemical properties of TiO_2 as anode material for LIBs: (**b**) CV curves at a scan rate of 0.1 mV s^{-1}; (**c**) cycling performance at a current density of 0.1 A g^{-1}, (**d**) GCD curves, (**e**) capacity retention and fitted linear curve; (**f**) rate performance from 0.1 A g^{-1} to 4.0 A g^{-1}.

The working Image of the half-cell with the $Fe_2O_3@TiO_2$ heterostructure as the anode is shown in Figure 4a. Firstly, the electrochemical reactions of the $Fe_2O_3@TiO_2$ heterostructure are explored by the CV test, with the CV curves from the first to third cycles shown in Figure 4b. During the initial discharge process, a prominent reduction peak at 1.72 V indicates the lithium-ion insertion into the TiO_2 shell, as described by Equation (2). Further, the second reduction peak at 0.77 V corresponds to the SEI film generation of TiO_2, echoing the reduction peak of SEI film generation in Figure 3b. During the first oxidation process, the oxidation peak ranging from 1.41 V to 2.42 V corresponds to the continuous transformation of Fe^0 to Fe^{3+}. In addition, the oxidation peak located at 2.1 V indicates the lithium-ion deinsertion from TiO_2, which is consistent with previous results. The positions of the oxidation/reduction peaks of the second cycle remain unchanged, indicating the

excellent electrical conductivity of the Fe_2O_3@TiO_2 heterostructure. The emergence of a new reduction peak at 0.92V in the second and third CV curves, a process shown in Equation (1), further substantiates the lithiation of Fe_2O_3. The broader reduction peak of Fe_2O_3 in the third CV curve compared to the second suggests a progressive and complete lithiation of Fe_2O_3. The CV test results imply that the Fe_2O_3@TiO_2 heterostructure engages in both lithium-ion insertion/deinsertion and reduction/oxidation, thereby demonstrating superior electrochemical stability. Figure 4c shows the short-term cycle performance of the Fe_2O_3@TiO_2 heterostructure at 0.1 A g^{-1}. During the initial insertion/desertion process, the discharge and charge capacities are recorded as 1869 mAh g^{-1} and 1697 mAh g^{-1}, respectively, resulting in an impressive ICE of 90.9%. The high discharge capacity is ascribed to the abundance of active lithium-ion storage sites on the disordered surface of TiO_2 and the enhanced charge transfer characteristics of Fe_2O_3. The high Coulomb efficiency is attributed to the synergistic effect after hybridization, which enhances the electrochemical reaction stability. The cycle curve reveals a gradual decrease in discharge capacity from the 1st cycle to the 50th cycle. Subsequently, the Fe_2O_3@TiO_2 heterostructure exhibits fluctuating discharge capacity around 1300 mAh g^{-1} after 30 cycles, ultimately reaching 1342 mAh g^{-1} at the 300th cycle. Furthermore, the electrochemical process is further explored through the GCD curves in Figure 4d. The GCD curve of the fifth cycle fits well with the 10th cycle and exhibits a large discharge platform from 1 V to 0.6 V, implying excellent electrical conductivity and structural stability of the Fe_2O_3@TiO_2 heterostructure. When compared with the GCD curves of Fe_2O_3, the Fe_2O_3@TiO_2 heterostructure shows better electrochemical stability and maintains a highly reversible electrochemical reaction during 300 cycles. The cycle durability of Fe_2O_3@TiO_2 heterostructure is verified by the capacity retention in Figure 4e. Compared with the first cycle, the capacity retention can exhibit 92.79% at 10 cycles, and it is stable at approximately 80% after the 50th cycle. Comparing the capacity retention of Fe_2O_3 and TiO_2, it can be observed that the capacity retention of the Fe_2O_3@TiO_2 heterostructure is significantly higher than both individual anodes due to their synergistic effect. Moreover, the TiO_2 shell effectively alleviates the volume expansion and successfully maintains the electrochemical activity of Fe_2O_3. The rate performance of the Fe_2O_3@TiO_2 heterostructure is exhibited in Figure 4f. The discharge capacity of the Fe_2O_3@TiO_2 heterostructure is 1297 mAh g^{-1} after 20 cycles at 0.1 A g^{-1}. Upon restoring the current density to 0.1 A g^{-1}, the discharge capacity can be reinstated to 1217 mAh g^{-1}. This result suggests that the built-in electric field can improve the lithium-ion reaction kinetics and the heterogeneous interface can provide more active sites for lithium-ion insertion. Figure S5a shows the cycle curve of the Fe_2O_3@TiO_2 heterostructure during 2000 cycles at 1.0 A g^{-1}. The initial cycle exhibits a remarkable discharge capacity of 1555 mAh g^{-1} and an impressive charge capacity of 1274 mAh g^{-1} for the Fe_2O_3@TiO_2 heterostructure. Compared with Fe_2O_3 and TiO_2, the ICE of the Fe_2O_3@TiO_2 heterostructure shows a great improvement of 82%. The enhanced electrochemical stability can be attributed to the protective effect of the core-shell structure, which effectively mitigates volume expansion. The discharge capacity reaches 736 mAh g^{-1}, while maintaining a consistent Coulomb efficiency of ~100% even after the 2000th cycle at 1.0 A g^{-1}. Compared with the long-term cycle properties shown in Figures 2a and 3, Fe_2O_3@TiO_2 heterostructure exhibits better capacity and more stable Coulomb efficiency. The capacity retention of the Fe_2O_3@TiO_2 heterostructure is calculated in Figure S5b. Compared to the first discharge capacity, the capacity retention of the 10th cycle is 80.73%, exhibiting a slight decrease in capacity retention before the 150th cycle. It is worth noting that between the 200th cycle and the 1600th cycle, the capacity retention rises and stabilizes at around 95%. Eventually, the capacity retention can still be maintained at 83.62% in the 2000th cycle. In summary, after a series of electrochemical tests, the Fe_2O_3@TiO_2 heterostructure has better lithium-ion storage capacity than Fe_2O_3 and TiO_2. Further, in order to comprehensively evaluate the lithium-ion storage performance of the Fe_2O_3@TiO_2 heterostructure, both the discharge capacity and cycle life for the iron-based anodes are collected in Table S1. Obviously, the Fe_2O_3@TiO_2 heterostructure achieves superior discharge capacity and cycle life compared

to other reported iron-based anodes, indicating its extensive application potential as an anode for LIBs. The higher discharge capacity is provided by the synergistic effect of the heterogeneous interface and abundant active lithium-ion storage sites. The smaller polarization phenomenon could be related to the improved electron/ion migration kinetics of the built-in electric field. The enhanced durability of the longer cycle contributes to effectively mitigating the volume expansion during repeated lithium-ion insertion/desertion, thereby showing the remarkable efficacy of the TiO$_2$ shell.
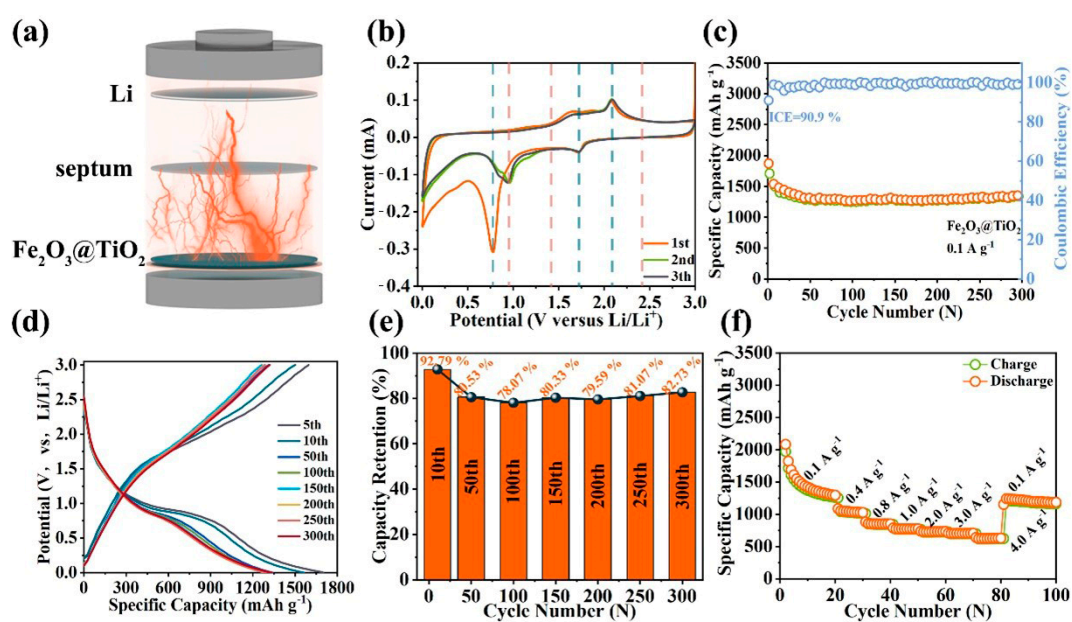
Figure 4. (**a**) Model image of half-cell. Electrochemical properties of Fe$_2$O$_3$@TiO$_2$ heterostructure as anode material for LIBs: (**b**) CV curves at a scan rate of 0.1 mV s^{-1}; (**c**) cycling performance at a current density of 0.1 A g^{-1}, (**d**) GCD curves, (**e**) capacity retention and fitted linear curve; (**f**) rate performance from 0.1 A g^{-1} to 4.0 A g^{-1}.

The pseudocapacitance behavior of the Fe$_2$O$_3$@TiO$_2$ heterostructure is investigated through CV testing at various scan rates. The CV curves of the Fe$_2$O$_3$@TiO$_2$ heterostructure at different scan rates are shown in Figure 5a. The observed trend suggests that, as the scan rate increases, the shape of the CV curves remains consistent. This observation provides strong evidence for high electrochemical stability and minimal polarization [40], which is consistent with the result of rate capacity.

$$i = av^b \qquad (3)$$

The *b*-value can be determined by the relationship between the current (*i*) and the scan rate (*v*), as depicted in Equation (3). *a* is a constant, thus the *b*-value can be calculated from the slope of log(*i*) and log(*v*) [41]. The *b*-value is a critical parameter for evaluating diffusion-controlled and surface capacitive-controlled processes. When the *b*-value is less than 0.5, the electrochemical reaction is diffusion progress; and when the *b*-value is higher than 1, the electrochemical reaction is completely capacitive behaviors [42]. For the oxidation peaks and reduction peaks belonging to the Fe$_2$O$_3$@TiO$_2$ heterostructure, *b*-values are calculated and linearly fitted, and the results are shown in Figure 5b. All *b*-values are between 0.5 and 1, indicating that pseudocapacitance behavior exists in the electrochemical process of the Fe$_2$O$_3$@TiO$_2$ heterostructure.
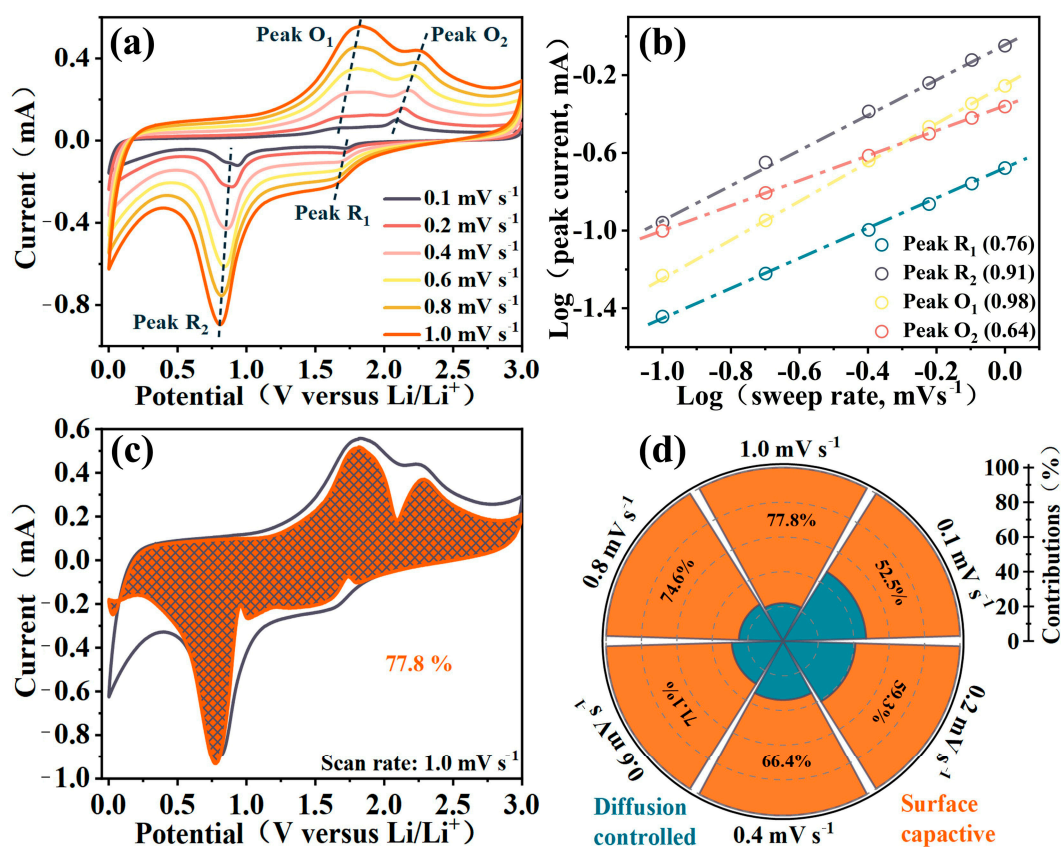
$$i = k_1 v + k_2 v^{1/2} \qquad (4)$$

Figure 5. (**a**) CV curves of $Fe_2O_3@TiO_2$ heterostructure at different scan rates from 0.1 to 1.0 mV s^{-1}; (**b**) the *b*-values of corresponding oxidation peaks and reduction peaks; (**c**) area ratio image of pseudocapacitance at 1.0 mV s^{-1}; (**d**) ratio image of pseudocapacitance contribution at different scan rates from 0.1 to 1.0 mV s^{-1}.

The behavior of pseudocapacitance can be quantitatively analyzed according to Equation (4) [43], where *i* is the current, and *v* is the scan rate. At a particular voltage, k_1 and k_2 can be treated as constants. According to the calculated results, Figure 5c shows the pseudocapacitance behavior ratio at 1.0 mV s^{-1}. In fact, the results demonstrate the proportion of pseudocapacitance behavior is as high as 77.8%, and high pseudocapacitance behavior can improve the lithium-ion reaction kinetics, which is consistent with the previous electrochemical analysis. Further, according to Figure 5d, pseudocapacitance behavior dominates the electrochemical process of $Fe_2O_3@TiO_2$ heterostructure. In addition, EIS analysis is further performed to investigate the electrical conductivity, shown in Figure S6. The fitted charge-transfer resistance of $Fe_2O_3@TiO_2$ (99.3 Ω) is much smaller than that of Fe_2O_3 (342.1 Ω) or TiO_2 (160.8 Ω), and the slope of $Fe_2O_3@TiO_2$ in the low-frequency region is larger, showing higher electronic conductivity. The reason for the high pseudocapacitance behavior and high electronic conductivity can be attributed to the disordered surface providing more active lithium-ion storage sites and the built-in electric field bringing more powerful electron/ion mobility.

3. Conclusions

In conclusion, the core-shell $Fe_2O_3@TiO_2$ heterostructure has been successfully prepared through heterointerface engineering. The well-designed heterogeneous interface between Fe_2O_3 and TiO_2 forms conventional p-n junctions, forming a built-in electric field that enhances electrochemical kinetics. The meticulously engineered core-shell structure effectively mitigates volumetric expansion and imparts exceptional cycling durability to the $Fe_2O_3@TiO_2$ heterostructure (capacity retention of 83.62% after 2000 cycles). The disor-

dered surface provides abundant active sites for lithium-ion storage (discharge capacity of 1342 mAh g^{-1} at 0.1 A g^{-1}), reducing the lithium-ion diffusion barrier and increasing the capacity. This study underscores the pivotal role of designing semiconducting heterostructures in enhancing electrochemical activity, thereby paving the way for novel applications of heterogeneous electrode materials.

References

1. Sun, C.; Chen, F.; Tang, X.; Zhang, D.; Zheng, K.; Zhu, G.; Bin Shahid, U.; Liu, Z.; Shao, M.; Wang, J. Simultaneous interfacial interaction and built-in electric field regulation of GaZnON@NG for high-performance lithium-ion storage. *Nano Energy* **2022**, *99*, 107369. [CrossRef]
2. Zhao, L.; Ning, Y.; Dong, Q.; Ullah, Z.; Zhu, P.; Zheng, S.; Xia, G.; Zhu, S.; Li, Q.; Liu, L. Longer cycle life and higher discharge voltage of a small molecular indanthrone resulting from the extended conjugated framework. *J. Power Sources* **2023**, *556*, 232518. [CrossRef]
3. Mostafa, M.M.M.; Alshehri, A.A.; Salama, R.S. High performance of supercapacitor based on alumina nanoparticles derived from Coca-Cola cans. *J. Energy Storage* **2023**, *64*, 107168. [CrossRef]
4. Yan, Z.; Li, J.; Chen, Q.; Chen, S.; Luo, L.; Chen, Y. Synthesis of CoSe$_2$/Mxene Composites Using as High-performance Anode Materials for Lithium-ion Batteries. *Adv. Compos. Hybrid Mater.* **2022**, *5*, 2977–2987. [CrossRef]
5. Zhu, Y.; Zhang, Y.; Das, P.; Wu, Z.-S. Recent Advances in Interface Engineering and Architecture Design of Air-Stable and Water-Resistant Lithium Metal Anodes. *Energy Fuels* **2021**, *35*, 12902–12920. [CrossRef]
6. Ma, J.; Zheng, S.; Zhou, F.; Zhu, Y.; Das, P.; Huang, R.; Zhang, L.; Wang, X.; Wang, H.; Cui, Y.; et al. All 3D printing lithium metal batteries with hierarchically and conductively porous skeleton for ultrahigh areal energy density. *Energy Storage Mater.* **2023**, *54*, 304–312. [CrossRef]
7. Zhao, Z.; Zhao, X.; Zhou, Y.; Liu, S.; Fang, G.; Liang, S. Towards establishing uniform metrics for evaluating the safety of lithium metal batteries. *Adv. Powder Mater.* **2023**, *2*, 100139. [CrossRef]
8. Ji, X.; Zhang, Y.; Cao, M.; Gu, Q.; Wang, H.; Yu, J.; Guo, Z.-H.; Zhou, X. Advanced inorganic/polymer hybrid electrolytes for all-solid-state lithium batteries. *J. Adv. Ceram.* **2022**, *11*, 835–861. [CrossRef]
9. Huang, J.; Dai, Q.; Cui, C.; Ren, H.; Lu, X.; Hong, Y.; Woo Joo, S. Cake-like porous Fe$_3$O$_4$@C nanocomposite as high-performance anode for Li-ion battery. *J. Electroanal. Chem.* **2022**, *918*, 116508. [CrossRef]

10. Miao, Z.; Li, D.; Zhao, L.; Gao, K.; Sun, W.; Zhao, W.; Yuan, L.; Zhang, H.; Li, Z.; Wang, Y.-J.; et al. Domain-limited Growth Strategy to Construct Fe$_3$C@C@CNTs Heterogeneous Interfaces for Multi-functional High-Performance Lithium-ion Storage and Microwave Absorption. *J. Alloys Compd.* **2023**, *967*, 171650. [CrossRef]

11. Yang, Z.; Zhu, P.; Ullah, Z.; Zheng, S.; Yu, S.; Zhu, S.; Liu, L.; Li, Q. Synchronous Light Harvesting and Energy Storing Organic Cathode Material 1,4-Dihydroxyanthraquinone for Lithium-Ion Batteries. *Chem. Eng. J.* **2023**, *468*, 143787. [CrossRef]

12. Li, Z.; Gao, K.; Han, Y.; Ding, S.; Cui, Y.; Hu, M.; Zhao, J.; Zhang, M.; Meng, A.; Yun, J.; et al. Atomic insights of electronic states engineering of GaN nanowires by Cu cation substitution for highly efficient lithium ion battery. *J. Energy Chem.* **2022**, *67*, 46. [CrossRef]

13. Kiran, L.; Aydinol, M.K.; Ahmad, A.; Shah, S.S.; Bahtiyar, D.; Shahzad, M.I.; Eldin, S.M.; Bahajjaj, A.A.A. Flowers Like a-MoO$_3$/CNTs/PANI Nanocomposites as Anode Materials for High-Performance Lithium Storage. *Molecules* **2023**, *28*, 3319. [CrossRef] [PubMed]

14. Kong, L.L.; Wang, L.; Sun, D.Y.; Meng, S.; Xu, D.D.; He, Z.X.; Dong, X.Y.; Li, Y.F.; Jin, Y.C. Aggregation-Morphology-Dependent Electrochemical Performance of Co$_3$O$_4$ Anode Materials for Lithium-Ion Batteries. *Molecules* **2019**, *24*, 3149. [CrossRef]

15. Liu, Y.L.; Yang, R.F.; Li, X.X.; Yang, W.S.; Lin, Y.W.; Zhang, G.Q.; Wang, L.J. Nb$_2$O$_5$ Coating to Improve the Cyclic Stability and Voltage Decay of Li-Rich Cathode Material for Lithium-Ion Battery. *Molecules* **2023**, *28*, 3890. [CrossRef]

16. Sun, C.; Xu, X.; Cui, C.; Chen, F.; Wang, Y.; Chen, S.; Shao, M.; Wang, J. High-Quality Epitaxial N Doped Graphene on SiC with Tunable Interfacial Interactions via Electron/Ion Bridges for Stable Lithium-Ion Storage. *Nano Micro Lett.* **2023**, *15*, 202. [CrossRef]

17. Li, L.; Xie, F.; Wu, H.; Zhu, Y.; Zhang, P.; Li, Y.; Li, H.; Zhao, L.; Zhu, G. N-Doped Porous Carbon-Nanofiber-Supported Fe$_3$C/Fe$_2$O$_3$ Nanoparticles as Anode for High-Performance Supercapacitors. *Molecules* **2023**, *28*, 5751. [CrossRef]

18. Li, H.; Jiang, J.; Huang, J.; Wang, Y.; Peng, Y.; Zhang, Y.; Hwang, B.-J.; Zhao, J. Investigation of the Na Storage Property of One-Dimensional Cu$_{2-x}$Se Nanorods. *ACS Appl. Mater. Interfaces* **2018**, *10*, 13491–13498. [CrossRef]

19. Chen, J.S.; Zhu, T.; Yang, X.H.; Yang, H.G.; Lou, X.W. Top-Down Fabrication of α-Fe$_2$O$_3$ Single-Crystal Nanodiscs and Microparticles with Tunable Porosity for Largely Improved Lithium Storage Properties. *J. Am. Chem. Soc.* **2010**, *132*, 13162–13164. [CrossRef]

20. Qi, X.; Zhang, H.-B.; Xu, J.; Wu, X.; Yang, D.; Qu, J.; Yu, Z.-Z. Highly Efficient High-Pressure Homogenization Approach for Scalable Production of High-Quality Graphene Sheets and Sandwich-Structured α-Fe2O3/Graphene Hybrids for High-Performance Lithium-Ion Batteries. *ACS Appl. Mater. Interfaces* **2017**, *9*, 11025–11034. [CrossRef]

21. Wang, W.; Feng, Y.; Zhang, S.; Wang, M.; Song, W.; Yue, L.; Ge, M.; Mi, J. Facile Premixed Flame Synthesis C@Fe$_2$O$_3$/SWCNT as Superior Free-standing Anode for Lithium-ion Batteries. *J. Alloys Compd.* **2022**, *905*, 164247. [CrossRef]

22. He, D.; Sun, M.; Cao, D.; Ding, Y.; Chen, H.; He, G. Flexible Free-Standing Fe2O3 Nanoparticle/Carbon Shells/Graphene Films for Advanced Lithium-Ion Batteries. *ACS Appl. Nano Mater.* **2022**, *5*, 5017–5024. [CrossRef]

23. Xu, J.-S.; Zhu, Y.-J. Monodisperse Fe$_3$O$_4$ and γ-Fe$_2$O$_3$ Magnetic Mesoporous Microspheres as Anode Materials for Lithium-Ion Batteries. *ACS Appl. Mater. Interfaces* **2012**, *4*, 4752–4757. [CrossRef] [PubMed]

24. Al-Thabaiti, S.A.; Mostafa, M.M.M.; Ahmed, A.I.; Salama, R.S. Synthesis of copper/chromium metal organic frameworks-Derivatives as an advanced electrode material for high-performance supercapacitors. *Ceram. Int.* **2023**, *49*, 5119–5129. [CrossRef]

25. Zhang, Y.; Ding, Z.; Foster, C.W.; Banks, C.E.; Qiu, X.; Ji, X. Oxygen Vacancies Evoked Blue TiO$_2$(B) Nanobelts with Efficiency Enhancement in Sodium Storage Behaviors. *Adv. Funct. Mater.* **2017**, *27*, 1700856. [CrossRef]

26. Xia, T.; Zhang, W.; Li, W.J.; Oyler, N.A.; Liu, G.; Chen, X.B. Hydrogenated Surface Disorder Enhances Lithium ion Battery Performance. *Nano Energy* **2013**, *2*, 826–835. [CrossRef]

27. Wang, L.; Yang, H.; Shu, T.; Xin, Y.; Chen, X.; Li, Y.; Li, H.; Hu, X. Nanoengineering S-Doped TiO$_2$ Embedded Carbon Nanosheets for Pseudocapacitance-Enhanced Li-Ion Capacitors. *ACS Appl. Energy Mater.* **2018**, *1*, 1708–1715. [CrossRef]

28. Hao, Z.; Chen, Q.; Dai, W.; Ren, Y.; Zhou, Y.; Yang, J.; Xie, S.; Shen, Y.; Wu, J.; Chen, W.; et al. Oxygen-Deficient Blue TiO$_2$ for Ultrastable and Fast Lithium Storage. *Adv. Energy Mater.* **2020**, *10*, 1903107. [CrossRef]

29. Li, J.; Wen, W.; Xu, G.; Zou, M.; Huang, Z.; Guan, L. Fe-added Fe$_3$C carbon nanofibers as anode for Li ion batteries with excellent low-temperature performance. *Electrochim. Acta* **2015**, *153*, 300. [CrossRef]

30. Cao, L.; Liang, X.; Ou, X.; Yang, X.; Li, Y.; Yang, C.; Lin, Z.; Liu, M. Heterointerface Engineering of Hierarchical Bi$_2$S$_3$/MoS$_2$ with Self-Generated Rich Phase Boundaries for Superior Sodium Storage Performance. *Adv. Funct. Mater.* **2020**, *30*, 1910732. [CrossRef]

31. Kresse, G.; Hafner, J. Ab Initio Molecular Dynamics for Open-shell Transition Metals. *Phys. Rev. B* **1993**, *48*, 13115–13118. [CrossRef]

32. Kresse, G.; Hafner, J. Ab initio molecular dynamics for liquid metals. *Phys. Rev. B* **1993**, *47*, 558–561. [CrossRef] [PubMed]

33. Pian, C.; Peng, W.; Ren, H.; Ma, C.; Su, Y.; Ti, R.; Chen, X.; Zhu, L.; Liu, J.; Sun, X.; et al. Robust α-Fe$_2$O$_3$@TiO$_2$ Core–Shell Structures with Tunable Buffer Chambers for High-Performance Lithium Storage. *Front. Chem.* **2022**, *10*, 866369. [CrossRef] [PubMed]

34. Li, Z.; Li, Y.; Xie, H.; Zuo, Z.; Chu, P. High electrochemical performance Li-ion batteries based on the porous carbon@Fe$_2$O$_3$ composite anode. *Ionics* **2022**, *28*, 4943–4947. [CrossRef]

35. Su, Q.; Xie, D.; Zhang, J.; Du, G.; Xu, B. In Situ Transmission Electron Microscopy Observation of the Conversion Mechanism of Fe$_2$O$_3$/Graphene Anode during Lithiation–Delithiation Processes. *ACS Nano* **2013**, *7*, 9115–9121. [CrossRef]

36. Huang, Y.; Xu, Z.; Mai, J.; Lau, T.-K.; Lu, X.; Hsu, Y.-J.; Chen, Y.; Lee, A.C.; Hou, Y.; Meng, Y.S.; et al. Revisiting the Origin of Cycling Enhanced Capacity of Fe_3O_4 Based Nanostructured Electrode for Lithium ion Batteries. *Nano Energy* **2017**, *41*, 426–433. [CrossRef]

37. Wang, Z.; Wang, Y.; Chen, Y.; Yousaf, M.; Wu, H.; Cao, A.; Han, R.P.S. Reticulate Dual-Nanowire Aerogel for Multifunctional Applications: A High-Performance Strain Sensor and a High Areal Capacity Rechargeable Anode. *Adv. Funct. Mater.* **2019**, *29*, 1807467. [CrossRef]

38. Zheng, H.; Yang, Y.; Liu, X.; Guo, Z.; Feng, C. Controllable synthesis of $FeVO_4$@TiO_2 nanostructures as anode for lithium ion battery. *J. Nanopart. Res.* **2017**, *19*, 243. [CrossRef]

39. Hayashi, A.; Hama, S.; Morimoto, H.; Tatsumisago, M.; Minami, T. Preparation of Li_2S–P_2S_5 Amorphous Solid Electrolytes by Mechanical Milling. *J. Am. Ceram. Soc.* **2001**, *84*, 477–479. [CrossRef]

40. Pu, X.; Zhao, D.; Fu, C.; Chen, Z.; Cao, S.; Wang, C.; Cao, Y. Understanding and Calibration of Charge Storage Mechanism in Cyclic Voltammetry Curves. *Angew. Chem. Int. Ed.* **2021**, *60*, 21310–21318. [CrossRef]

41. Chen, M.; Chao, D.; Liu, J.; Yan, J.; Zhang, B.; Huang, Y.; Lin, J.; Shen, Z.X. Rapid Pseudocapacitive Sodium-Ion Response Induced by 2D Ultrathin Tin Monoxide Nanoarrays. *Adv. Funct. Mater.* **2017**, *27*, 1606232. [CrossRef]

42. Chen, C.; Wen, Y.; Hu, X.; Ji, X.; Yan, M.; Mai, L.; Hu, P.; Shan, B.; Huang, Y. Na^+ intercalation pseudocapacitance in graphene-coupled titanium oxide enabling ultra-fast sodium storage and long-term cycling. *Nat. Commun.* **2015**, *6*, 6929. [CrossRef]

43. Xia, X.; Chao, D.; Zhang, Y.; Zhan, J.; Zhong, Y.; Wang, X.; Wang, Y.; Shen, Z.X.; Tu, J.; Fan, H.J. Generic Synthesis of Carbon Nanotube Branches on Metal Oxide Arrays Exhibiting Stable High-Rate and Long-Cycle Sodium-Ion Storage. *Small* **2016**, *12*, 3048–3058. [CrossRef] [PubMed]

44. Liu, Z.; Yu, X.-Y.; Paik, U. Etching-in-a-Box: A Novel Strategy to Synthesize Unique Yolk-Shelled Fe_3O_4@Carbon with an Ultralong Cycling Life for Lithium Storage. *Adv. Energy Mater.* **2016**, *6*, 1502318. [CrossRef]

45. Wang, L.; Chen, Q.; Zhu, Y.; Qian, Y. Graphene-wrapped Fe_2O_3 nanorings for Li ion battery anodes. *Chin. Sci. Bull.* **2014**, *59*, 4271–4273. [CrossRef]

46. Lin, Y.; Sun, L.; Hu, J.; Tan, H.; Xie, F.; Qu, Y.; Wang, K.; Zhang, Y. Ti-doped Fe_2O_3/carbon cloth anode with oxygen vacancies and partial rGO encapsulation for flexible lithium ion batteries. *J. Alloys Compd.* **2022**, *924*, 166441. [CrossRef]

47. Luo, Y.; Luo, J.; Jiang, J.; Zhou, W.; Yang, H.; Qi, X.; Zhang, H.; Fan, H.J.; Yu, D.Y.W.; Li, C.M.; et al. Seed-assisted synthesis of highly ordered TiO_2@α-Fe_2O_3 core/shell arrays on carbon textiles for lithium-ion battery applications. *Energy Environ. Sci.* **2012**, *5*, 6559–6566. [CrossRef]

48. Lv, X.; Deng, J.; Sun, X. Cumulative effect of Fe_2O_3 on TiO_2 nanotubes via atomic layer deposition with enhanced lithium ion storage performance. *Appl. Surf. Sci.* **2016**, *369*, 314–319. [CrossRef]

49. Chen, M.; Li, W.; Shen, X.; Diao, G. Fabrication of Core–Shell α-Fe_2O_3@ $Li_4Ti_5O_{12}$ Composite and Its Application in the Lithium Ion Batteries. *ACS Appl. Mater. Interfaces* **2014**, *6*, 4514–4523. [CrossRef]

50. Su, L.; Zhong, Y.; Zhou, Z. Role of Transition Metal Nanoparticles in the Extra Lithium Storage Capacity of Transition Metal Oxides: A Case Study of Hierarchical Core–shell Fe_3O_4@C and Fe@C Microspheres. *J. Mater. Chem. A* **2013**, *1*, 15158–15166. [CrossRef]

51. Ding, R.; Zhang, J.; Zhang, J.; Li, Z.; Wang, C.; Chen, M. Core-shell Fe_2N@amorphous carbon nanocomposite-filled 3D graphene framework: An additive-free anode material for lithium-ion batteries. *Chem. Eng. J.* **2019**, *360*, 1063–1070. [CrossRef]

52. Li, Y.; Fu, Y.; Chen, S.; Huang, Z.; Wang, L.; Song, Y. Porous Fe_2O_3/Fe_3O_4@Carbon octahedron arrayed on three-dimensional graphene foam for lithium-ion battery. *Compos. Part B* **2019**, *171*, 130–137. [CrossRef]